Optik - International Journal for Light and Electron Optics 267 (2022) 169652

Contents lists available at ScienceDirect

Optik

journal homepage: www.elsevier.com/locate/ijleo

Concurrent topology and fiber orientation optimization of CFRP structures in space-borne optical remote sensor

B. Huang [a,b,*], Z.H. Li [a], X.Z. Tian [a], L. Yang [a], C.Y. Han [a], B. Chen [a]

[a] Changchun Institute of Optics, Fine Mechanics and Physics, Chinese Academy of Science, Changchun, Jilin 130031, China
[b] University of Chinese Academy of Science, Beijing 100039, China

ARTICLE INFO

Keywords:
Fiber orientation optimization
Topology optimization
Space-borne optical remote sensor
Constitutive matrix
CFRP

ABSTRACT

Lightweight design is one of the most important concepts in the design of space-borne optical remote sensors. Carbon fiber reinforced polymer (CFRP), as one material with high ratio of modulus to density, is widely employed to realize the lightweight design. To maximize the stiffness and strength of CFRP with prescribed mass, fiber orientation and topology optimization are accomplished and optimum design result is acquired in this paper. First, the optimization algorithm of fiber orientation is put forward to find the optimal fiber direction and verified by theoretical analysis and simulations, illustrating that [90°/+ 45°/− 45°/0°] fiber orientation and symmetrical laminas are indispensable. Furthermore, the topology optimization algorithm including the density interpolation method and sensitivity analysis method is brought about to find the optimal material distribution. The algorithm is validated to be convergent and can provide a conceptual model which offers a reference for the critical design. Finally, acquired in the mechanical test is the performance of the optical remote sensor whose first three characteristic frequencies are respectively 66.95 Hz, 70.37 Hz, and 98.84 Hz. The mechanical amplification factor is 5.29, which meet the performance requirement of the stiffness and strength for the optical remote sensor.

1. Introduction

Carbon fiber reinforced polymer (CFRP), as a type of composite materials of fiber reinforcement, has gained a considerable reputation and application in lots of industries such as aerospace, automotive and other fields due to its high stiffness and modulus even when compared with some metal materials [1–4]. CFRP is a kind of anisotropic materials whose performance is much dependent on the fiber orientation. Besides, topology and size design also have a significant influence on the stiffness of a CFRP component. Therefore, a large amount of research work has been so far concentrated on the CFRP optimization of fiber orientation, topology and size design among scholars and institutes all over the world.

As to the optimization of fiber orientation, R. Matsuzaki optimized the composite plates with curvilinear fiber orientation in order to obtain a unique mechanical property [5]. C. Nguyen and Y. Choi utilized Euler angles to represent the fiber orientation in a rigid coordinate system and performed a fiber orientation optimization to enhance the mechanical property of functionally graded conformal lattice structures [6]. B. Krour presented a new method to reduce the interfacial stress concentration by taking the effect of

* Corresponding author at: Changchun Institute of Optics, Fine Mechanics and Physics, Chinese Academy of Science, Changchun, Jilin 130031, China.

E-mail address: huangbin@ciomp.ac.cn (B. Huang).

https://doi.org/10.1016/j.ijleo.2022.169652
Received 6 May 2022; Received in revised form 9 July 2022; Accepted 12 July 2022
Available online 16 July 2022
0030-4026/

Table 1
System parameters and performance indices.

No.	Item	Requirement
1	Travel range	Pitch axis: $\pm$ 34.5° Azimuth axis: $-$ 33.5°$\sim$+ 7°
2	Total mass	$\leq$ 75 kg
3	Natural frequency	$\geq$ 50 Hz
4	Moment of inertia	Pitch axis$\leq$ 4 kg·m^2 Azimuth axis$\leq$ 3.2 kg·m^2

fiber orientation into consideration [7]. Z. Rasheva studied the correlation between the mechanical properties and fiber orientation, and the results show that the fiber orientation of carbon fibers is playing a critical role in optimizing the mechanical performance of CFRP [8]. Usually, there are two common technique employed to conduct the optimization of fiber orientation, namely analytical solutions based on laminate theories [9–14] and numerical simulation by finite element modeling in computer-aided engineering software [15–20]. Great progress has been made in fiber orientation optimization while little effort has been devoted to the field that the effect of fiber orientation on the thermal and mechanical performances can also be investigated by taking into account the constitutive tensor of CFRP structure, which is the function of Euler angles [21–24].

Topology optimization, a very process of determining the connectivity, shape and location of voids inside a given design domain, has become a notably powerful design technique, which has great influence in early conceptual and preliminary design and impacts the performance of the final structure [25–30]. In the past few decades, numerous topology modeling methodologies were put forward, such as density-based methods [31–33], evolutionary structural optimization method [34,35] and level set method [36,37]. Density-based methods are the most widely used due to their intuitive mathematical expressions and physical meaning, among which Solid Isotropic Material with Penalization (SIMP) [38–40] and Ramp Approximation of Material Properties (RAMP) [41] are two most popular modeling methodologies. Together with modeling methods, optimization algorithms available in topology optimization, including Sequential Quadratic Programming (SQP) [42,43], Method of Moving Asymptotes (MMA) [44,45] and Optimization Criterion Method (OCM) [46–48], have been under discussions in the recent several years. Nevertheless, too little work has been devoted to the application of all the methodologies and algorithms to space-borne optical remote sensors and aircrafts.

In this paper, a novel type of space-borne optical remote sensor is demonstrated which works to image the X-rays and extreme ultraviolet (EUV) radiated from the sun. The majority of mechanical components of the optical remote sensor are manufactured with CFRP material. Therefore, several key factors that have a noticeably positive influence on the enhancement of mechanical performance are investigated. To analyze the influence of fiber orientations on mechanical performance, presented is a novel method in which constitutive matrix of CFRP and Euler transformation matrix which is the function of fiber orientation are both introduced. Furthermore, SIMP, as the most popular modeling method in topology optimization, and sensitivity analysis method are both demonstrated. That is a novel application since these two methodologies have up till now received extremely little attention in aerospace industry. Moreover, accomplished are numerical simulations including fiber orientation optimization, topology optimization of a critical mechanical component of the optical remote sensor, and frequency response analysis of the instrument. Finally, the results of mechanics test are provided in a close agreement with the numerical simulation, validating the effectiveness of the methodologies and algorithms and the correctness of the numerical simulation results.

The remainder of this paper is organized as follows. A system description about the optical remote sensor including performance index and geometrical model is presented in Section 2. In Section 3, the mathematical model of fiber orientation is established and the numerical simulation is conducted. In Section 4, the algorithms of topology optimization are demonstrated and the topology optimization model of U-frame, one critical mechanical component, is set up in Hypermesh. Furthermore, frequency response analysis of the instrument is described in this section including the modal analysis and sinusoidal excitation analysis. The results and discussions of mechanics test are presented in Section 5. In Section 6, a conclusion is drawn.

2. System description

2.1. Performance index

In order to forecast the space weather and earth weather, solar corona-X-rays and extreme ultraviolet (EUV) radiated from the sun-is needed to be observed. As a result, a novel type of space-borne optical remote sensor is developed to image X-rays and EUV. System parameters and performance indices of this optical remote sensor that have an influence on the structural design are presented in Table 1.

2.2. Geometrical model

According to the system requirement illustrated in Table 1, the optical remote sensor is required to comprise two degrees of freedom with large travel range and to be in light weight. After comparing specific stiffness of all the most widely used materials, CFRP is found to be with the highest ratio of stiffness to density, so it is the most appropriate material for the majority of mechanical components of the imager.

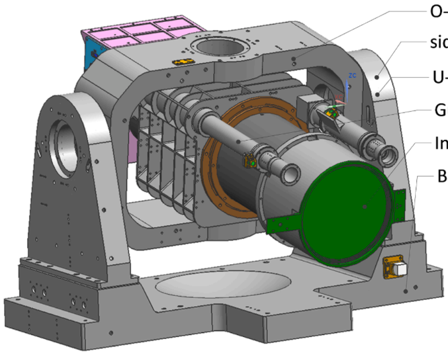

Fig. 1. Geometrical model of optical remote sensor.

The critical mechanical components of the optical remote sensor include U-frame, O-frame and some other structures, of which the U-frame is the primary component analyzed as an example in this paper. The U-frame includes one base and two side-legs. An optical imager, as the core instrument of the optical sensor, is mounted on the O-frame and rotates along the azimuth and pitch axis. The imager and the O-frame are both mounted on the U-frame. The geometrical model is shown in Fig. 1.

3. Fiber orientation optimization

3.1. Modeling and formulation

A classical topology optimization problem of CFRP consists of finding the optimum layout of material and the local reinforced direction CFRP is oriented to maximize the stiffness of the CFRP component. In this section, the density of component, namely the distribution of material, is constant while the local reinforced vector of fiber orientation within a given volume is a optimization variable to minimize the compliance, namely the inverse of stiffness in another word.

The topology optimization problem including material distribution and fiber orientation can be described mathematically in Eq. (1).

$$Minimize: c(\rho,\theta) = \mathbf{u}(\rho,\theta)^{\mathrm{T}}\mathbf{f} \tag{1}$$

$$Subjectto: \begin{cases} \dfrac{V(\rho)}{V_0} \leq frac \\ \mathbf{K}(\rho,\theta)\mathbf{u}(\rho,\theta) = \mathbf{f} \\ \rho_{\min} \leq \rho \leq 1 \\ -\dfrac{\pi}{2} \leq \theta < \dfrac{\pi}{2} \end{cases} \tag{2}$$

Next, all the parameters in the equations are explained. The compliance c is the objective function in the optimization, as a function of density and fiber orientation. $\mathbf{u}(\rho,\theta)$ is a column vector denoting the displacement of all nodes and $\boldsymbol{f}$ is also a column vector denoting the load applied to all the nodes in finite element model. The first constraint in Eq.(2) is imposed on the design volume $V(\rho)$ limiting to a prescribed volume fraction *frac* ($0 \leq f \leq 1$). The second constraint imposes equilibrium on the design volume that the stiffness matrix $\mathbf{K}(\rho,\theta)$ and displacement vector $\mathbf{u}(\rho,\theta)$ are design-independent and it is assumed that the applied load $\boldsymbol{f}$ is not a function of density and fiber orientation. Moreover, the third and the fourth constraints included in Eq.(2) are simple bounds on element density and fiber orientation, namely the element material angle. The former imposes a lower bound of $\rho_{\min}$ on element density to avoid singularity issues in the finite element stiffness matrix $\mathbf{K}(\rho,\theta)$.

Since the density of element is constant in this section, Eq.(1) and Eq.(2) can be simplified as follows.

$$Minimize: c(\theta) = \mathbf{u}(\theta)^{\mathrm{T}}\mathbf{K}(\theta)\mathbf{u}(\theta)\left(-\frac{\pi}{2} \leq \theta < \frac{\pi}{2}\right) \tag{3}$$

The stiffness matrix $K(\theta)$ is assembled by contributions from each element stiffness matrix $k_e(\theta)$ as given in Eq.(4).

$$\mathbf{K}(\theta) = \sum_{e=1}^{N}\mathbf{k_e}(\theta) \tag{4}$$

where N denotes the number of finite elements. Then the Eq.(3) can be written in terms of element stiffness matrix $k_e(\theta)$ and element displacement $u_e(\theta)$, which simplifies the evaluation of compliance in the optimization calculations by making it an element-by-element computation

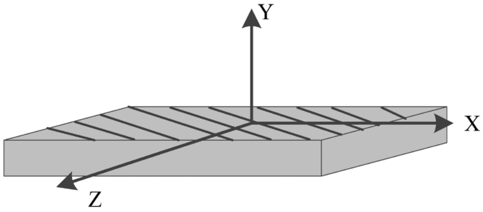

Fig. 2. Laminate coordinate system.

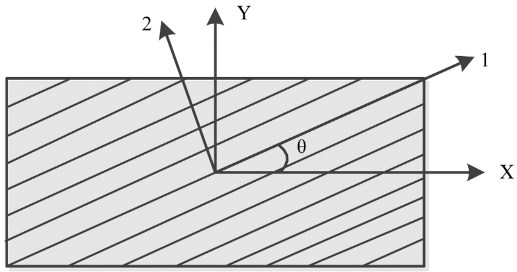

Fig. 3. lamina coordinate system.

$$c(\theta) = \sum_{e=1}^{N} \mathbf{u_e}(\theta)^{\mathrm{T}} \mathbf{k_e}(\theta) \mathbf{u_e}(\theta) \tag{5}$$

The element stiffness matrix in Eq.(5) is obtained in the usual way where element integrations are performed in the prescribed design volume.

$$\mathbf{k_e} = \int_{\Omega_d} \mathbf{B}^{\mathrm{T}} \overline{\mathbf{Q}}(\theta) \mathbf{B} \mathrm{d}\Omega_d \tag{6}$$

where B is the strain-displacement matrix defined by derivatives of the element shape functions and $Q(—)(\theta)$ is denoted as the rotated constitutive matrix in terms of original constitutive matrix $Q(\theta)$. The calculation of $Q(—)(\theta)$ is demonstrated in detail.

According to the laminate theory, two kinds of coordinate systems are employed to describe the laminate direction and fiber direction—the laminate coordinate system where x-axis represents the primary axis and the lamina coordinate system where 1-axis represents the fiber orientation. Both are depicted in Fig. 2 and Fig. 3 respectively.

Since the fiber orientation optimization is simplified to a 2-dimensional problem, the relationship between stress and strain can be presented as follows.

$$\begin{bmatrix} \sigma_1 \\ \sigma_1 \\ \tau_{12} \end{bmatrix} = \begin{bmatrix} Q_{11} & Q_{12} & 0 \\ Q_{12} & Q_{22} & 0 \\ 0 & 0 & Q_{66} \end{bmatrix} \begin{bmatrix} \varepsilon_1 \\ \varepsilon_2 \\ \gamma_{12} \end{bmatrix} \tag{7}$$

Where $[D]$ is the original constitutive matrix in which.

$Q_{11} = \frac{E_1}{1-\nu_{12}\nu_{21}}, Q_{12} = \frac{\nu_{12}E_2}{1-\nu_{12}\nu_{21}} = \frac{\nu_{21}E_1}{1-\nu_{12}\nu_{21}}, Q_{22} = \frac{E_2}{1-\nu_{12}\nu_{21}}, Q_{66} = G_{12}.$

It is known that CFRP is a kind of transversely isotropic materials so the Poisson's ratio ν_{12} and ν_{21} in two directions are not equal to each other.

Particularly, when there is a rotation between laminate and lamina coordinate systems shown in the Fig. 3, the relationship of stress and strain in these two frames is Eq.(8) and Eq.(9).

$$\begin{bmatrix} \sigma_x \\ \sigma_y \\ \tau_{xy} \end{bmatrix} = \mathbf{T} \begin{bmatrix} \sigma_1 \\ \sigma_1 \\ \tau_{12} \end{bmatrix} \tag{8}$$

$$\begin{bmatrix} \varepsilon_x \\ \varepsilon_y \\ \frac{\gamma_{xy}}{2} \end{bmatrix} = \mathbf{T} \begin{bmatrix} \varepsilon_1 \\ \varepsilon_2 \\ \frac{\gamma_{12}}{2} \end{bmatrix} \tag{9}$$

Therefore, the stress and strain in laminate coordinate system and the rotated constitutive matrix can satisfy the following equation

$$\begin{bmatrix} \sigma_x \\ \sigma_y \\ \tau_{xy} \end{bmatrix} = [\overline{\mathbf{Q}}] \begin{bmatrix} \varepsilon_x \\ \varepsilon_y \\ \gamma_{xy} \end{bmatrix} = \begin{bmatrix} \overline{Q_{11}} & \overline{Q_{12}} & \overline{Q_{16}} \\ \overline{Q_{12}} & \overline{Q_{22}} & \overline{Q_{26}} \\ \overline{Q_{16}} & \overline{Q_{26}} & \overline{Q_{66}} \end{bmatrix} \begin{bmatrix} \varepsilon_x \\ \varepsilon_y \\ \gamma_{xy} \end{bmatrix} \tag{10}$$

According to Eq.(11), it can be calculated that

$$\overline{\mathbf{Q}}(\theta) = \mathbf{T}(\theta)\mathbf{Q}(\theta)\mathbf{T}^{\mathrm{T}}(\theta) \tag{11}$$

where $\boldsymbol{T}(\theta)$ is the transformation matrix in terms of fiber angle and presented as follows.

$$\mathbf{T}(\theta) = \begin{bmatrix} a_{11}^2 & a_{12}^2 & a_{13}^2 & 2a_{12}a_{13} & 2a_{13}a_{11} & 2a_{11}a_{12} \\ a_{21}^2 & a_{22}^2 & a_{23}^2 & 2a_{22}a_{23} & 2a_{23}a_{21} & 2a_{21}a_{22} \\ a_{31}^2 & a_{32}^2 & a_{33}^2 & 2a_{32}a_{33} & 2a_{33}a_{31} & 2a_{31}a_{32} \\ a_{12}a_{31} & a_{22}a_{32} & a_{23}a_{33} & a_{22}a_{33}+a_{23}a_{32} & a_{21}a_{33}+a_{23}a_{31} & a_{22}a_{31}+a_{21}a_{32} \\ a_{31}a_{11} & a_{32}a_{12} & a_{33}a_{13} & a_{12}a_{33}+a_{13}a_{32} & a_{13}a_{31}+a_{11}a_{33} & a_{11}a_{32}+a_{12}a_{31} \\ a_{11}a_{21} & a_{12}a_{22} & a_{13}a_{23} & a_{12}a_{23}+a_{13}a_{22} & a_{13}a_{21}+a_{11}a_{23} & a_{11}a_{22}+a_{12}a_{21} \end{bmatrix} \tag{12}$$

where all the elements a_{ij} ($i = 1,2,3$; $j = 1,2,3$) are from another rotated matrix $T'(\theta)$ which is also with respect to fiber angle. Furthermore, without losing generality, it is assumed that the fiber rotation is along 3-axis in lamina coordinate system, then $T'(\theta)$ can be demonstrated as in Eq.(9).

$$\mathbf{T}'(\theta) = \begin{bmatrix} \cos\theta & -\sin\theta & 0 \\ \sin\theta & \cos\theta & 0 \\ 0 & 0 & 1 \end{bmatrix} \tag{13}$$

Consequently, $T(\theta)$ is simplified as follows in Eq.(10).

$$\mathbf{T}(\theta) = \begin{bmatrix} \cos^2\theta & \sin^2\theta & 0 & 0 & 0 & -2\sin\theta\cos\theta \\ \sin^2\theta & \cos^2\theta & 0 & 0 & 0 & 2\sin\theta\cos\theta \\ 0 & 0 & 1 & 0 & 0 & 0 \\ 0 & 0 & 0 & \cos\theta & \sin\theta & 0 \\ 0 & 0 & 0 & -\sin\theta & \cos\theta & 0 \\ \sin\theta\cos\theta & -\sin\theta\cos\theta & 0 & 0 & 0 & \cos^2\theta-\sin^2\theta \end{bmatrix} \tag{14}$$

which can be as well simplified further to a 3×3 matrix since the fiber orientation optimization is a 2-dimensional problem. Therefore, $[T]$ is transformed as follows.

$$\mathbf{T}(\theta) = \begin{bmatrix} \cos^2\theta & \sin^2\theta & -2\sin\theta\cos\theta \\ \sin^2\theta & \cos^2\theta & 2\sin\theta\cos\theta \\ \sin\theta\cos\theta & -\sin\theta\cos\theta & \cos^2\theta-\sin^2\theta \end{bmatrix} \tag{15}$$

Based on the equations from Eq.(10) to Eq.(15), the constitutive matrix of a rotated carbon fiber can be acquired as follows.

$$\begin{cases} \overline{Q}_{11} = Q_{11}\cos^4\theta + (2Q_{12}+4Q_{66})\sin^2\theta\cos^2\theta + Q_{22}\sin^4\theta \\ \overline{Q}_{12} = (Q_{11}+Q_{22}-4Q_{66})\sin^2\theta\cos^2\theta + Q_{12}(\sin^4\theta+\cos^4\theta) \\ \overline{Q}_{16} = (Q_{11}\cos^2\theta + Q_{22}\sin^2\theta + Q_{12} - 2Q_{66}\cos 2\theta)\sin\theta\cos\theta \\ \overline{Q}_{22} = Q_{11}\sin^4\theta + (2Q_{12}+4Q_{66})\sin^2\theta\cos^2\theta + Q_{22}\cos^4\theta \\ \overline{Q}_{26} = (Q_{11}\sin^2\theta + Q_{22}\cos^2\theta - Q_{12}\cos 2\theta + 2Q_{66}\cos 2\theta)\sin\theta\cos\theta \\ \overline{Q}_{66} = (Q_{11}+Q_{22}-2Q_{12})\sin^2\theta\cos^2\theta + Q_{66}\cos^2 2\theta \end{cases} \tag{16}$$

The relationship between stress and strain in the lamina coordinate system has been discussed in detail. In addition, the relationship between stress and strain in the laminate coordinate system also needs to be demonstrated.

According to the relationship between stress and strain in laminate theory, the total strain in the laminate coordinate system is

$$\begin{bmatrix} \varepsilon_x \\ \varepsilon_y \\ \gamma_{xy} \end{bmatrix} = \begin{bmatrix} \varepsilon_x^0 \\ \varepsilon_y^0 \\ \gamma_{xy}^0 \end{bmatrix} + Z \begin{bmatrix} k_x \\ k_y \\ k_{xy} \end{bmatrix} \tag{17}$$

where.

$[\varepsilon_x, \varepsilon_y, \varepsilon_z]^T$ denotes the strain in an arbitrary lamina;.

$[\varepsilon_x^0, \varepsilon_y^0, \varepsilon_z^0]^T$ the strain in the neutral lamina;.

$[k_x, k_y, k_z]^T$ the curvature of the arbitrary lamina;.

Z the distance from the arbitrary lamina to the neutral lamina.

Table 2
Characteristic parameters.

Symbol	Characteristic parameter	Theoretical value
E_1	Longitudinal modulus (GPa)	290
E_2	Transversal modulus (GPa)	9
G	Shear modulus (GPa)	5
ν_{12}	Poisson' ratio	0.3

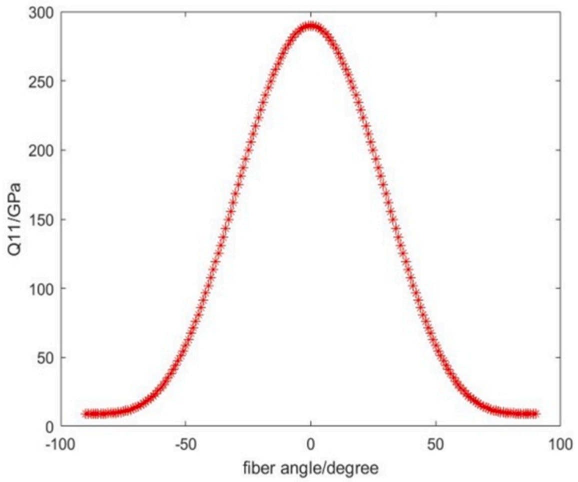

Fig. 4. $Q(—)_{11}$ and fiber angle.

By combining the Eq.(10) and Eq.(17), the relationship between stress and strain in the laminate coordinate system can be acquired as follows.

$$\begin{bmatrix}\sigma_x\\\sigma_y\\\tau_{xy}\end{bmatrix}=\begin{bmatrix}\overline{Q}_{11}&\overline{Q}_{12}&\overline{Q}_{16}\\\overline{Q}_{12}&\overline{Q}_{22}&\overline{Q}_{26}\\\overline{Q}_{16}&\overline{Q}_{26}&\overline{Q}_{66}\end{bmatrix}\left\{\begin{bmatrix}\varepsilon_x^0\\\varepsilon_y^0\\\gamma_{xy}^0\end{bmatrix}+Z\begin{bmatrix}k_x\\k_y\\k_{xy}\end{bmatrix}\right\} \tag{18}$$

Moreover, the relationship between the strain and the external loads including forces and moments in the laminate is

$$\left\{\begin{matrix}\mathbf{N}\\\mathbf{M}\end{matrix}\right\}=\begin{bmatrix}\mathbf{A}&\mathbf{B}\\\mathbf{B}&\mathbf{D}\end{bmatrix}\left\{\begin{matrix}\boldsymbol{\varepsilon}^0\\\mathbf{k}^0\end{matrix}\right\} \tag{19}$$

where.

N denotes the external tensile and shear force per unit length $[N_x, N_y, N_{xy}]^T$ with unit [N/m];.

M denotes the external bending moment and torque per unit length $[M_x, M_y, M_{xy}]^T$ with unit [N].

Matrix A, B and D, called respectively tensile stiffness matrix, coupling stiffness matrix and bending stiffness matrix, are three important matrices that influence the property and performance of CFRP depending on the parameter design, the definitions of which are

$$\begin{cases}\mathbf{A}=\sum_{k=1}^{n}\left(\overline{Q}_{ij}\right)_k\left(Z_k-Z_{k-1}\right)\\\mathbf{B}=-\frac{1}{2}\sum_{k=1}^{n}\left(\overline{Q}_{ij}\right)_k\left(Z_k^2-Z_{k-1}^2\right)\\\mathbf{D}=\frac{1}{3}\sum_{k=1}^{n}\left(\overline{Q}_{ij}\right)_k\left(Z_k^3-Z_{k-1}^3\right)\end{cases} \tag{20}$$

where Z_k denotes the coordinate of the top face of the k^{th} lamina on the z-axis in the laminate coordinate system whose origin and O-XY plane lie in the middle surface.

As is mentioned, matrix B is the coupling stiffness between the tensile stiffness and bending stiffness and matrix B is supposed to be

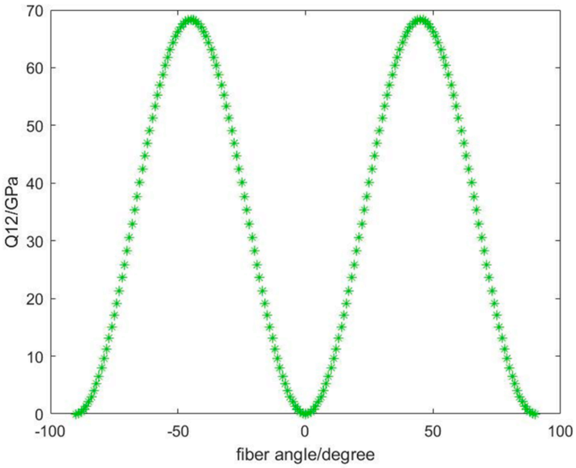

Fig. 5. $Q(—)_{12}$ and fiber angle.

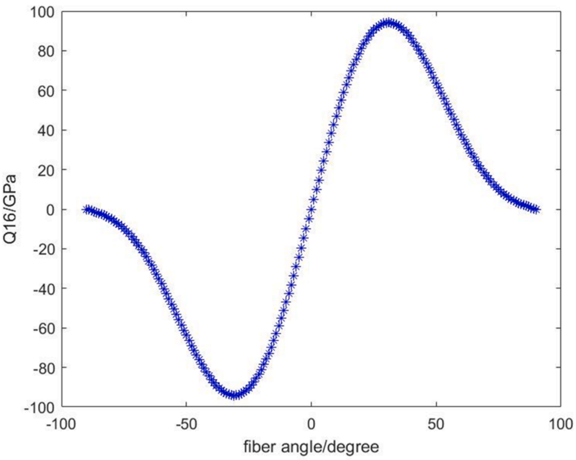

Fig. 6. $Q(—)_{16}$ and fiber angle.

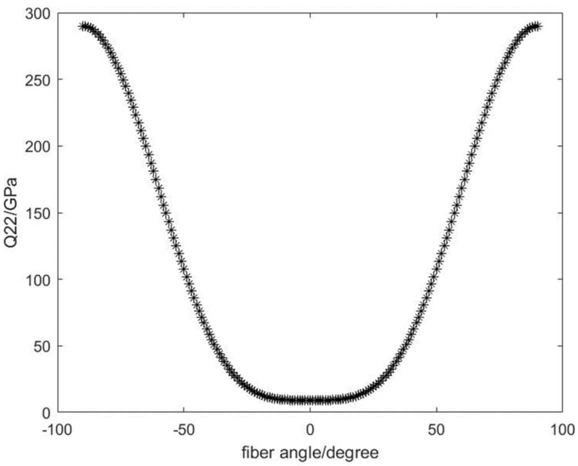

Fig. 7. $Q(—)_{22}$ and fiber angle.

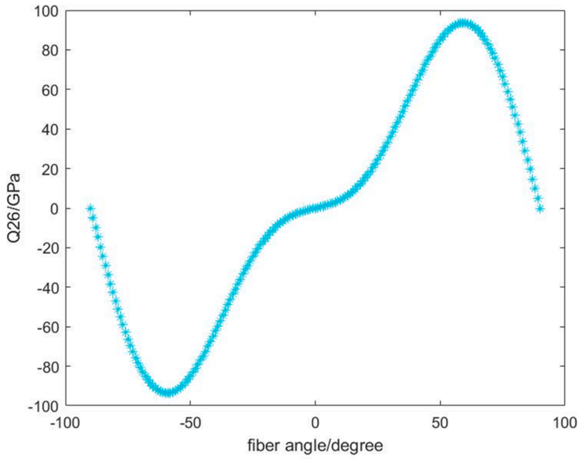

Fig. 8. $Q(—)_{26}$ and fiber angle.

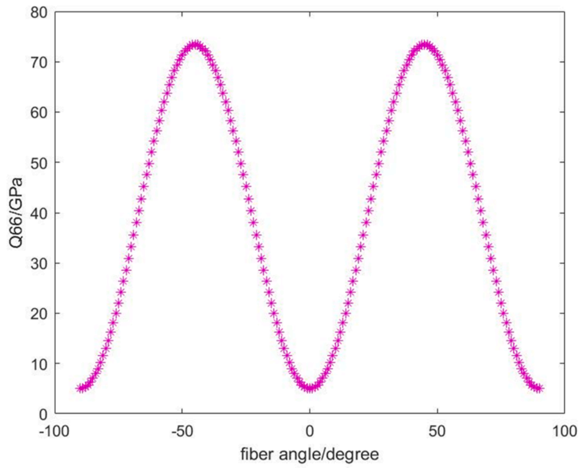

Fig. 9. $Q(—)_{66}$ and fiber angle.

designed to be a zero matrix such that there is no coupling between normal strain and shear strain. Hence, the laminate is supposed to be symmetric about its middle surface. As a result, the strain vector in Eq.(19) can be expressed as in Eq.(21).

$$\begin{bmatrix} \boldsymbol{\varepsilon}^0 \\ \mathbf{k}^0 \end{bmatrix} = \begin{bmatrix} \mathbf{A}^{-1} & 0 \\ 0 & \mathbf{D}^{-1} \end{bmatrix} \begin{bmatrix} \mathbf{N} \\ \mathbf{M} \end{bmatrix} \tag{21}$$

3.2. Numerical simulation

In the design of this space-borne optical remote sensor, some kind of CFRP with ultra high elastic modulus is employed, whose characteristic parameters are listed in Table2.

Based on Table2 and Eq.(7), it can be known that $Q_{11} = 290$ GPa, $Q_{12} = 2.7$ GPa, $Q_{22} = 9$ GPa, $Q_{66} = 5$ GPa. Therefore, the function curve of $Q(—)_{\mathrm{ij}}(\theta)$ with respect to θ can be gained as shown from Figs. 4–9. $Q(—)_{11}$ and $Q(—)_{22}$ are responsible for the normal stiffness of x-axis and y-axis and $Q(—)_{66}$ is responsible for the shear stiffness in the 0-xy plane in the laminate coordinate system. The other three items are coupling components between normal strain and shear strain. The former three components are the critical factors in the process of fiber orientation optimization.

The results in the figures imply that the maximums of $Q(—)_{11}$ and $Q(—)_{22}$ happen when the orientation is respectively $0^\circ$and 90°while the maximum of $Q(—)_{66}$ happens when the orientation is $\pm 45^\circ$. So the fiber orientation of laminas is optimized to 0°, $\pm 45^\circ$and 90°, which is in accordance with the most widely employed orientation of CFRP design.

Based on the aforementioned conclusions and in the Section 3.1, the fiber orientations should be 0°, $\pm 45^\circ$and 90°, and they are supposed to be symmetric about the neutral layer. Consequently, one kind of CFRP material with $[90^\circ/+45^\circ/-45^\circ/0^\circ/-45^\circ/+45^\circ/$

Define laminate:

Name	Id	Color	Material	Thickness	Orientati...	IP	Result
ply1	1		M55J	0.30000	90.0	3	yes
ply2	2		M55J	0.30000	45.0	3	yes
ply3	3		M55J	0.30000	-45.0	3	yes
ply4	4		M55J	0.30000	0.0	3	yes
ply5	5		M55J	0.30000	-45.0	3	yes
ply6	6		M55J	0.30000	45.0	3	yes
ply7	7		M55J	0.30000	90.0	3	yes

Fig. 10. Thickness and orientation of each lamina.

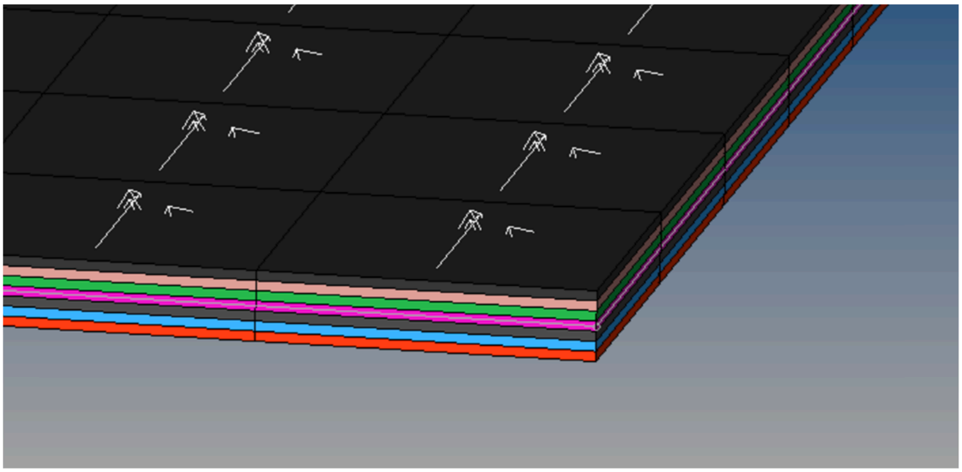

Fig. 11. Finite element model of the laminate.

90°] fiber orientation is analyzed with its finite element model established in Hypermesh. Its performance on every direction is also simulated in Hypermesh and compared with the analytical result.

Without losing generality, the thickness of each lamina is assumed to be 0.3 mm and the matrix A and D can be acquired according to Eq.(20).

$$\mathbf{A} = \begin{bmatrix} 189.7200 & 82.0125 & 0 \\ 82.0125 & 274.0200 & 0 \\ 0 & 0 & 92.5800 \end{bmatrix} \mathrm{GPa \cdot mm} \tag{22}$$

$$\mathbf{D} = \begin{bmatrix} 83.0817 & 57.2037 & 36.9846 \\ 57.2037 & 494.6765 & 36.3285 \\ 36.9846 & 36.3285 & 68.8270 \end{bmatrix} \mathrm{GPa \cdot mm^3} \tag{23}$$

Then the strain vector under the unit force and moment is depicted in Eq.(24).

$$\begin{bmatrix} \boldsymbol{\varepsilon}^0 \\ \mathbf{k}^0 \end{bmatrix} = \begin{bmatrix} 0.0061 & -0.0018 & 0 & & & \\ -0.0018 & 0.0042 & 0 & & 0 & \\ 0 & 0 & 0.0108 & & & \\ & & & 0.0166 & -0.0013 & -0.0082 \\ & 0 & & -0.0013 & 0.0022 & -0.0005 \\ & & & -0.0082 & -0.0005 & 0.0192 \end{bmatrix} \begin{bmatrix} 1 \\ 1 \\ 0 \\ 1 \\ 1 \\ 0 \end{bmatrix} = \begin{bmatrix} 0.0043\mu \\ 0.0024\mu \\ 0 \\ 0.0153\mu \\ 0.0009\mu \\ 0.0089\mu \end{bmatrix} \tag{24}$$

Furthermore, the finite element model of this kind of CFRP material is established in Hypermesh. The fiber orientation and the thickness of each lamina is set in Fig. 10.

The finite element model of the laminate with seven laminas is shown in Fig. 11, together with the orientation of each lamina with

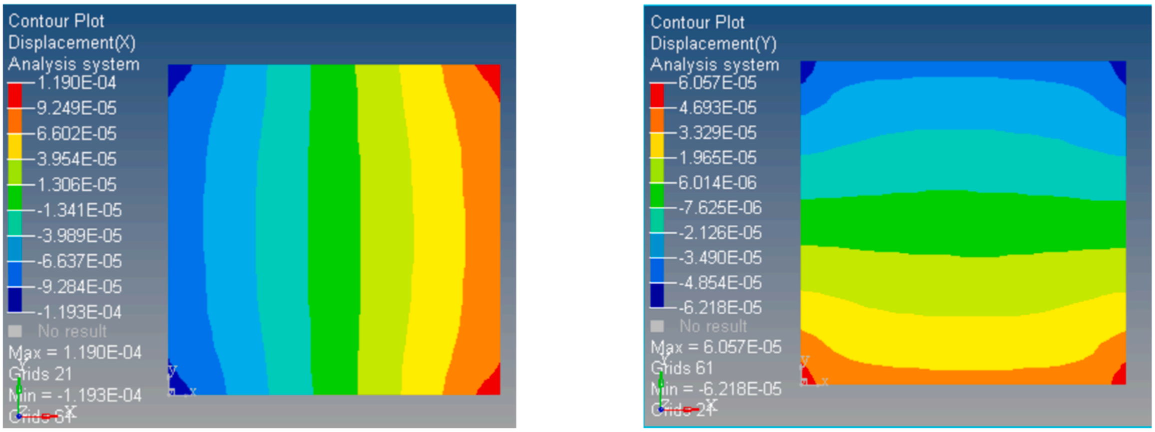

Fig. 12. Deformation analysis results.

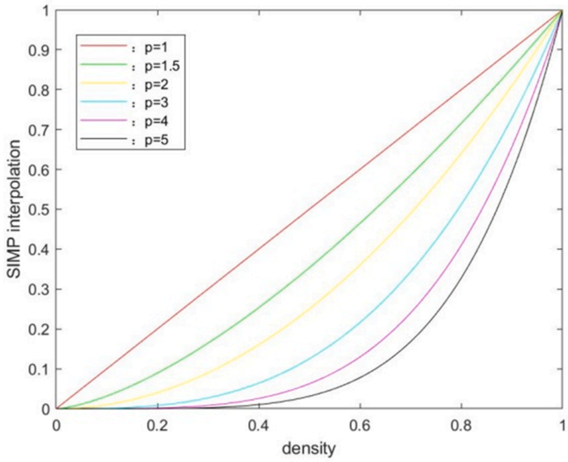

Fig. 13. Scheme of SIMP interpolation function.

respect to the laminate coordinate system.

Once the finite element model is obtained, a unit force array and a unit moment array are applied on the model to acquire the strain on each direction. The analysis results are illustrated in Fig. 12.

According to the deformation results, the displacement of x-direction is 1.19e-4 mm with the strain 0.0056μ and the displacement of y-direction is 6.057e-5 with the strain 0.0028μ, which are both in accordance with the theoretical calculations. Therefore, the correctness of the optimization model of carbon fiber orientation is validated by the calculation and simulation.

4. Topology optimization

4.1. Mathematical model

The goal of topology optimization is to find the optimal distribution of material to maximize the stiffness of a component and several algorithms with respect to topology optimization are presented including finite element modeling and sensitivity analysis.

4.1.1. SIMP

According to Eq.(1), it is known that there are two design variables in the CFRP topology optimization, the material distribution and fiber orientation. Since the optimal fiber orientation can be obtained, it is required that the optimal material distribution be found.

In order to determine that an element is solid or void, a critical aspect is the selection of an appropriate density interpolation function and penalization technique to express the physical quantities of the problem as a function of continuous design variables. Solid Isotropic Material with Penalization (SIMP), one of most popular finite element modeling algorithms, is a power function in terms of density with a constant penalty factor p as follows. The interpolation and penalization scheme of SIMP is shown in Fig. 13.

$$\eta(\rho) = \rho^p \tag{25}$$

After bringing in the SIMP density interpolation function, the objective function of topology optimization in Eq.(5) can be modified as follows.

$$c(\rho) = \sum_{e=1}^{N} \mathbf{u_e}(\rho)^{\mathrm{T}} \left[\rho^p \mathbf{k_e}(\rho)\right] \mathbf{u_e}(\rho) \tag{26}$$

4.1.2. Sensitivity analysis

Sensitivity analysis is one necessary and critical step in topology optimization because it helps figure out which part of material distribution the objective function is sensitive to, thus accelerating the convergence process. To calculate the sensitivity of compliance, the well-known adjoint method is adopted and the adjoint function is constructed firstly as follows.

$$c = \mathbf{u}^{\mathrm{T}}\mathbf{f} - \mathbf{s}^{\mathrm{T}}(\mathbf{Ku} - \mathbf{f}) \tag{27}$$

where **s** is an arbitrary real vector then the sensitivity of compliance to design variable is

$$\frac{\partial c}{\partial \rho_e} = \left(\mathbf{f}^{\mathrm{T}} - \mathbf{s}^{\mathrm{T}}\mathbf{K}\right)\frac{\partial \mathbf{u}}{\partial \rho_e} - \mathbf{s}^{\mathrm{T}}\frac{\partial \mathbf{K}}{\partial \rho_e}\mathbf{u} \tag{28}$$

In Eq.(28), vector **s** is assumed to be equal to **u** since **s** is arbitrary then the sensitivity of compliance can be simplified as follows.

$$\frac{\partial c}{\partial \rho_e} = -\mathbf{u}^{\mathrm{T}}\frac{\partial \mathbf{K}}{\partial \rho_e}\mathbf{u} \tag{29}$$

In Eq.(29), K denotes the global stiffness matrix of mechanical component and it can be described with respect to element stiffness matrix which is relative to element geometry matrix $\boldsymbol{B}$ and elasticity matrix $\boldsymbol{Q}$

$$\mathbf{K} = \sum_{i=1}^{Nele} \int_{Vele} \mathbf{B}^{\mathrm{T}}\mathbf{QB}dV_{\mathrm{ele}} \tag{30}$$

then

$$\frac{\partial \mathbf{K}}{\partial \rho_e} = \sum_{i=1}^{Nele} p\rho_e^{p-1} \int_{Vele} \mathbf{B}^{\mathrm{T}}\mathbf{Q}_0\mathbf{B}dV_{\mathrm{ele}} \tag{31}$$

where $\boldsymbol{Q}_0$ denotes the original elastic matrix and p is a penalty factor which can be assigned according to the analysis requirement. Therefore, the derivative of K with respect to element density ρ_e can be acquired by summation of each element.

The sensitivity of natural frequency can be derived by directly differentiating the characteristic equation with respect to design variable. Given the characteristic equation in Eq.(30), the sensitivity expression is Eq.(31).

$$(\mathbf{K} - \lambda_j\mathbf{M})\mathbf{\Phi}_j = 0 \tag{32}$$

$$\left(\mathbf{K} - \lambda_j\mathbf{M}\right)\frac{\partial \mathbf{\Phi}_j}{\partial \rho_e} = \frac{\partial \lambda_j}{\partial \rho_e}\mathbf{M\Phi}_j + \lambda_j\frac{\partial \mathbf{M}}{\partial \rho_e}\mathbf{\Phi}_j - \frac{\partial \mathbf{K}}{\partial \rho_e}\mathbf{\Phi}_j \tag{33}$$

where $\boldsymbol{M}$ denotes the global mass matrix and $\mathbf{\Phi}_j$ denotes the j^th^ eigenvector with respect to the j^th^ eigenvalue λ_j. It is known that ${\mathbf{\Phi}_j}^{\mathrm{T}}\mathbf{M\Phi}_j = 1$ after the orthogonal normalization of mass matrix so Eq.(32) can be obtained by pre-multiplying ${\mathbf{\Phi}_j}^{\mathrm{T}}$ on both sides of Eq.(31),

$${\mathbf{\Phi}_j}^{\mathrm{T}}\left(\mathbf{K} - \lambda_j\mathbf{M}\right)\frac{\partial \mathbf{\Phi}_j}{\partial \rho_e} = \frac{\partial \lambda_j}{\partial \rho_e}{\mathbf{\Phi}_j}^{\mathrm{T}}\mathbf{M\Phi}_j + \lambda_j{\mathbf{\Phi}_j}^{\mathrm{T}}\frac{\partial \mathbf{M}}{\partial \rho_e}\mathbf{\Phi}_j - {\mathbf{\Phi}_j}^{\mathrm{T}}\frac{\partial \mathbf{K}}{\partial \rho_e}\mathbf{\Phi}_j \tag{34}$$

Consequently, the sensitivity of natural frequency can be expressed as follows after simplification as

$$\frac{\partial \lambda_j}{\partial \rho_e} = {\mathbf{\Phi}_j}^{\mathrm{T}}\left(\frac{\partial \mathbf{K}}{\partial \rho_e} - \lambda_j\frac{\partial \mathbf{M}}{\partial \rho_e}\right)\mathbf{\Phi}_j \tag{35}$$

As to fiber orientation optimization, the mass M is a constant and the derivative of M with respect to element density is equal to zero. Then the Eq.(35) can be calculated according to Eq.(31).

$$\frac{\partial \lambda_j}{\partial \rho_e} = {\mathbf{\Phi}_j}^{\mathrm{T}}\frac{\partial \mathbf{K}}{\partial \rho_e}\mathbf{\Phi}_j \tag{36}$$

Additionally in the topology optimization, the derivative of M with respect to element density is

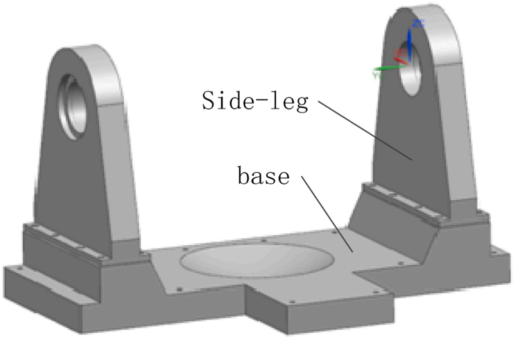

Fig. 14. Conceptual structure of the U-frame.

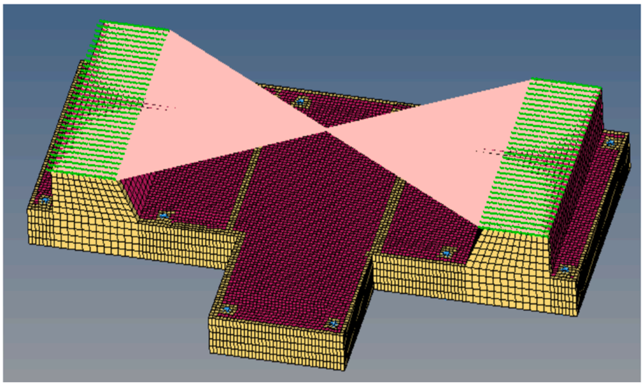

Fig. 15. Finite element model of the base.

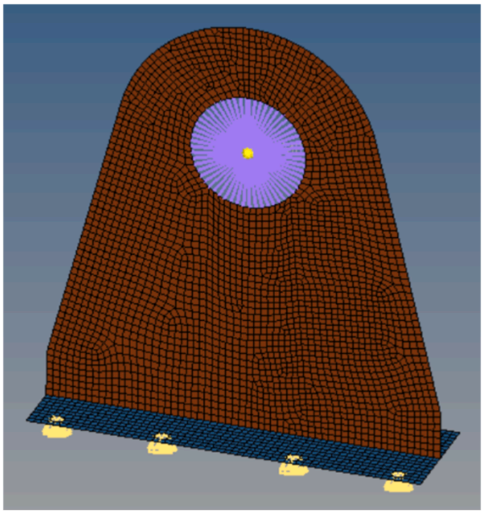

Fig. 16. Finite element model of the side-leg.

$$\frac{\partial \mathbf{M}}{\partial \rho_e} = \sum_{i=1}^{Nele} V_{\mathrm{i}} \tag{37}$$

Hence, Eq.(35) can be calculated with simultaneous equations of Eq.(31) and Eq.(37) and the sensitivity of compliance and natural frequency are acquired.

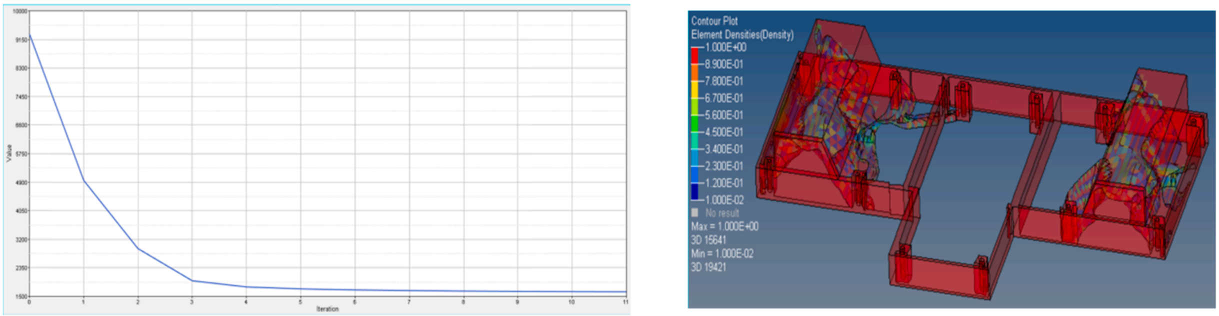

(a) Iteration curve (b) Analysis nephogram

Fig. 17. Optimization result of the base.

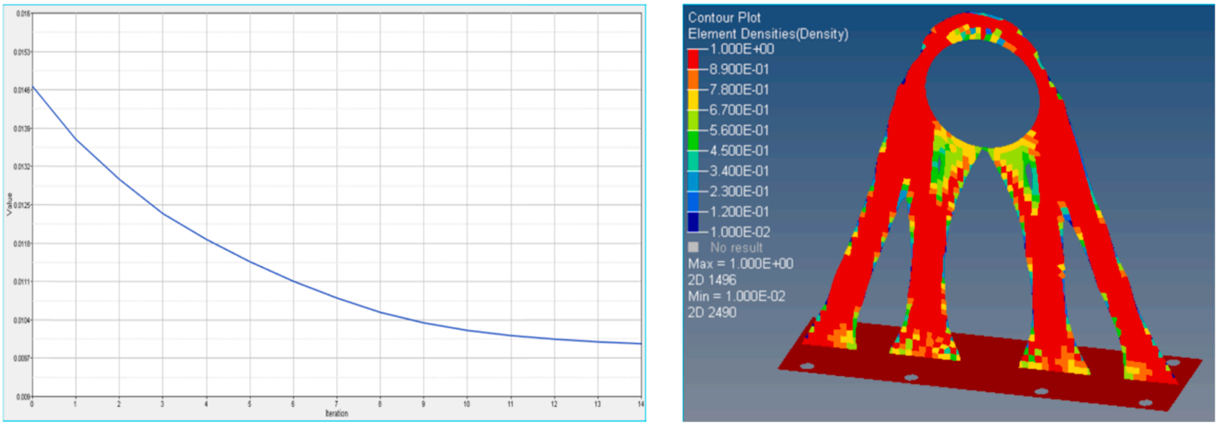

(a) Iteration curve (b) Analysis nephogram

Fig. 18. Optimization result of the side-leg.

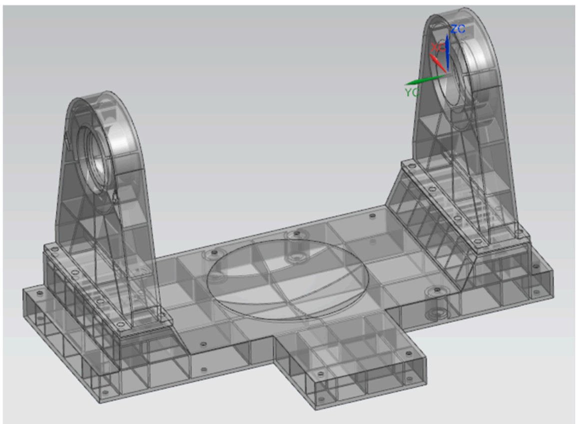

Fig. 19. Design result of U-frame.

4.2. Numerical simulation

In this section, the U-frame, as an example, is optimized with the aforementioned topology optimization algorithms and the finite element model is established in Hypermesh. To simplify the numerical analysis process, CFRP in this section is viewed as isotropic material and this simplification has little influence on the final analysis results.

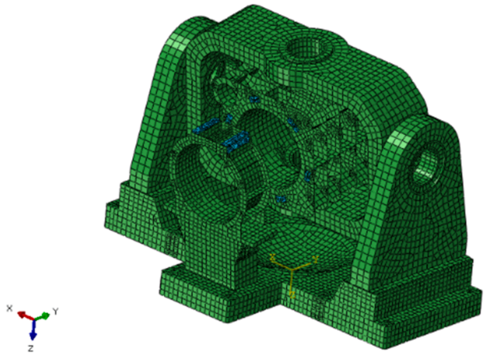

Fig. 20. Finite element model of the optical remote sensor.

The U-frame comprises two parts, the base and the side-leg. The conceptual structure model is given in Fig. 14.

The topology optimization models of the base and the side-leg are created and the element size is 5 mm. The optimization constraints include the static displacement of one critical node, the base frequency, and volume fraction. The static displacement of one critical node represents the shaft stiffness, the characteristic frequency of the remote sensor in another word, which is one of the most important performances of the instrument. The optimization objective is the minimum of the compliance of the whole component, the maximum of the stiffness in another word. The finite element models of the two components are respectively shown in Fig. 15 and Fig. 16.

As to the load case of the model in Fig. 15, fixed support is placed on 12 mounting holes and the nodes of two mounting surfaces are coupled with one critical node which represents the displacement of side-legs. Then design region and non-design region are introduced. Finally, the static and modal analysis are conducted.

In Fig. 16, the side-leg is a symmetrical component so the analysis calculation is simplified by extracting the neutral surface. As to the load case, the fixed support is placed on 8 mounting holes and the nodes of bearing mounting place are coupled with one critical node that represents the displacement of the shaft and bearings. Other analysis procedure is the same as the model in Fig. 15.

After several optimization iterations, the objective value is converged and the feasible design is acquired, and topology optimization results of these two components are depicted in Fig. 17 and Fig. 18.

Therefore, the structural design of the U-frame is determined based on the optimization results, in which the elements that contribute more to the stiffness of the structure are retained and the else are removed. The final design results are illustrated in Fig. 19.

4.3. Frequency response analysis

After the process of optimization design, the whole structure of the optical remote sensor is determinate. Frequency response analysis is a critical procedure to make sure that the stiffness and the strength of the structure can meet the performance requirement, validating the effectiveness of the optimization algorithm at the same time. This section of work includes two parts, modal analysis and sinusoidal excitation analysis.

4.3.1. Modal analysis

Modal analysis is employed to ensure that the stiffness of the optical remote sensor is enough such that the coupled vibration with the satellite will not happen for the instrument. The finite element model in modal analysis comprises all the crucial mechanical components, such as base, U-frame, and O-frame, as shown in Fig. 20.

The characteristic frequency and the color nephogram are listed in Table 3. It can be seen from the results that the first characteristic frequency is 92.6 Hz—a local mode, demonstrating that the stiffness of the instrument can meet the performance requirement.

4.3.2. Sinusoidal excitation

Sinusoidal excitation is the other critical work to make sure that the strength of all the materials used in the remote sensor can meet the requirement. The deformation results are depicted in Table 4 and the deformation color nephograms are presented in Table 5. According to the result, the deformation on X-direction is 0.387 mm with 1.5 g acceleration, Y-direction 1.419 mm with 1.5 g acceleration, and Z-direction 0.088 mm with 2.5 g acceleration. Hence, it can be calculated that the mechanical amplification factors on each direction are respectively.

Moreover, the maximum longitudinal stress, transverse stress and shear stress are 329.6 MPa, 9.2 MPa, and 3.1 MPa, respectively, which are all within the strength of the CFRP employed in the structure.

5. Results and discussion

Topology and structure of the optical remote sensor are both determined after the topology optimization and finite element simulation. Furthermore, to verify the correctness and effectiveness of the whole theoretical work, mechanical test of the optical

Table 3
Modal analysis results.

Mode	Frequency	Color nephogram
Mode 1	92.6 Hz	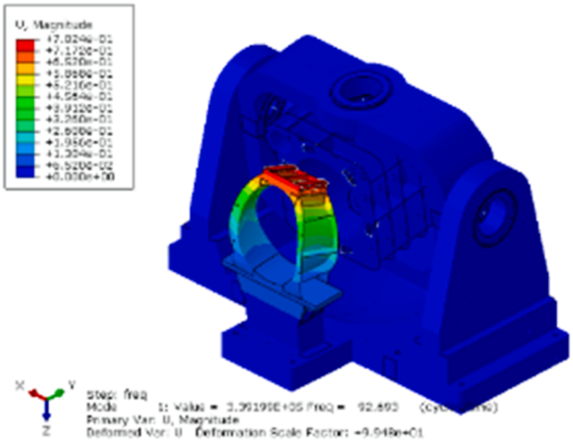
Mode 2	113.3 Hz	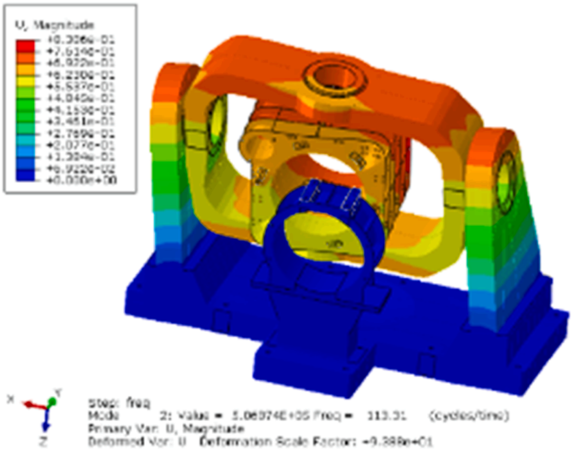
Mode 3	141.2 Hz	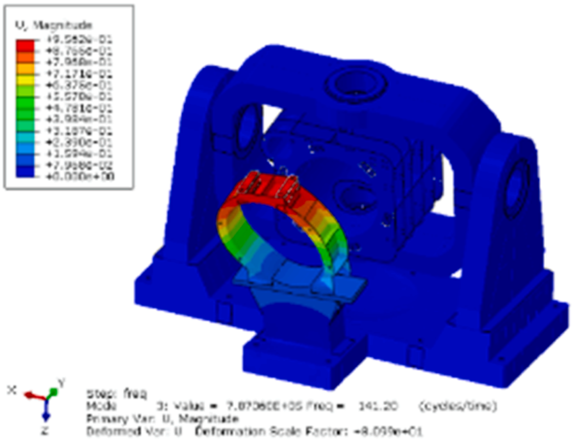
Mode 4	143.7 Hz	

(continued on next page)

Table 3 (*continued*)

Mode	Frequency	Color nephogram
		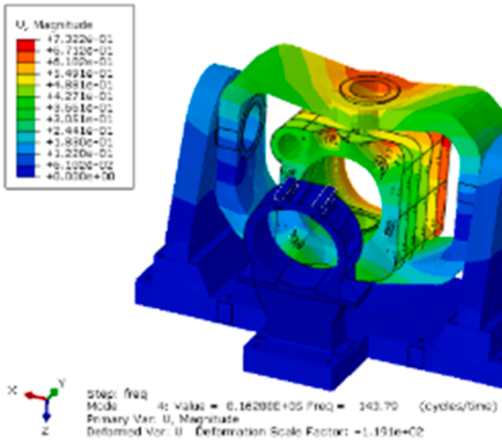

Table 4
Deformation results.

	UX (mm)	UY (mm)	UZ (mm)	USUM (mm)
X	0.387	0.106	0.068	0.387
Y	0.242	1.419	0.555	1.429
Z	0.012	0.065	0.088	0.090

Table 5
Deformation color nephograms.

X	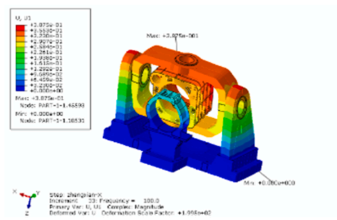	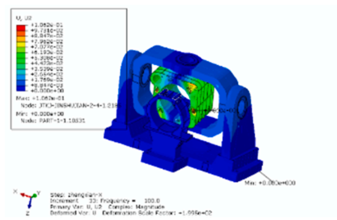	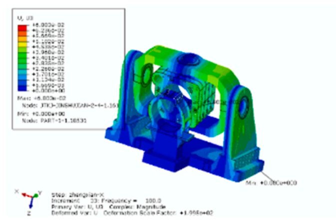
Y	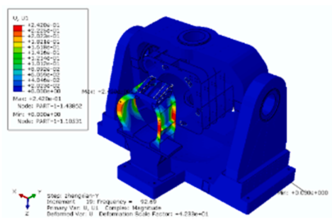	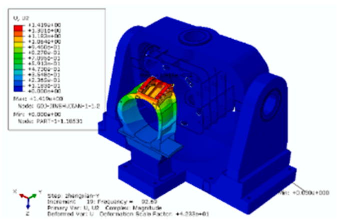	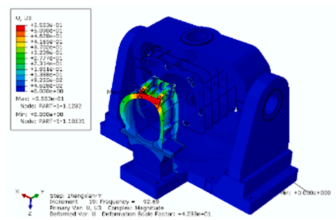
Z	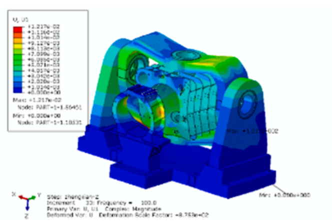	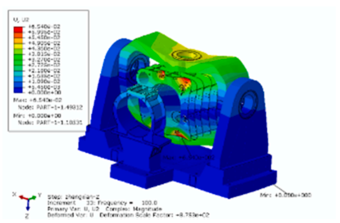	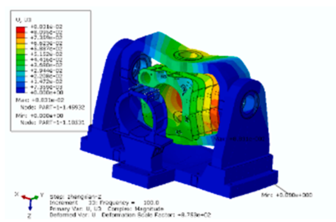

remote sensor is carried out in the laboratory. The test environment is shown in Fig. 21.

There are two kinds of acceleration transducers employed in the test—controlling transducer and measuring transducer. Controlling transducer is used for measuring the actual output of the vibration exciter to realize the closed-loop control and measuring

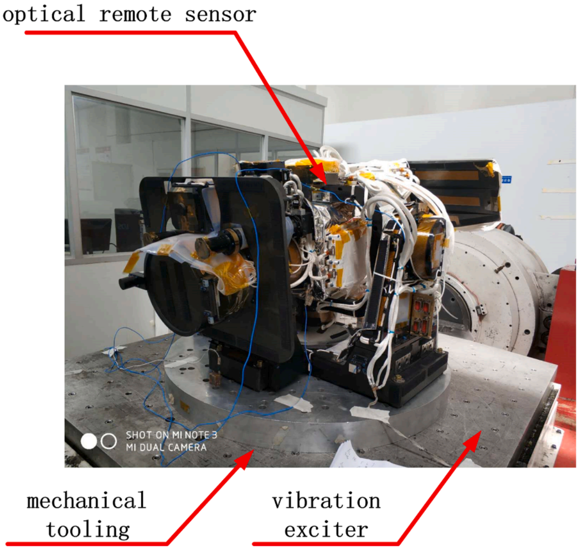

Fig. 21. Test environment.

Table 6
Test condition of sinusoidal excitation.

Frequency (Hz)	5–12	12–30	30–40	40–70	70–75	75–100		
Magnitude (0~P)	2.59 mm	1.5 g	1.5 g~2.0 g	2 g	2 g~1.5 g	1.5 g		
Direction	X-axis							
Sweep frequency speed	4oct/min							
Frequency (Hz)	5–12			12–100				
Magnitude (0~P)	2.59 mm			1.5 g				
Direction	Y-axis							
Sweep frequency speed	4oct/min							
Frequency (Hz)	5–12	12–35	35–40	40–50	50–55	55–75	75–80	80–100
Magnitude (0~P)	2.59 mm	1.5 g	1.5 g ~2.5 g	2.5 g	2.5 g~1.5 g	1.5 g	1.5 g~2.5 g	2.5 g
Direction	Z-axis							
Sweep frequency speed	4oct/min							

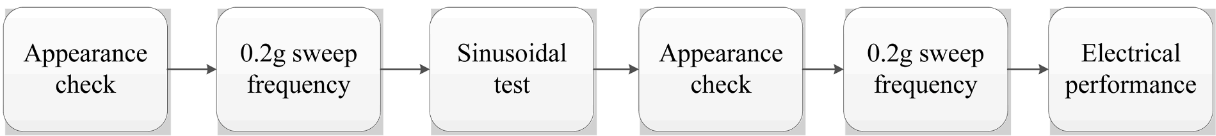

Fig. 22. Test process of sinusoidal excitation.

transducer is for measuring the response of some important components under the input signal. The test condition of sinusoidal excitation is listed in Table 6.

There are several steps in the mechanical test. Firstly, the appearance of the optical remote sensor is checked and sweeping frequency test with 0.2 g acceleration is accomplished to acquire the characteristic frequency and mechanical amplification factor. Then the sinusoidal test is conducted. After the aforementioned procedure, the appearance check and sweeping frequency test are repeated once more to make sure that the optical remote sensor is in good condition after the mechanical test. Finally, electrical performance test is done to verify that all the functions work well. The test process is illustrated in Fig. 22.

The characteristic frequency and mechanical amplification factor on each direction are acquired, which are listed in Table 7. According to the result, the characteristic frequency on X-direction is 66.95 Hz and the corresponding mechanical amplification factor is 5.29. The characteristic frequency on Y-direction is 98.84 Hz and the corresponding mechanical amplification factor is 4.058. The characteristic frequency on X-direction is 70.37 Hz and the corresponding mechanical amplification factor is 6.537.

According to the test result, the first three characteristic frequencies are respectively 66.95 Hz, 70.37 Hz, and 98.84 Hz while the simulation result is 92.6 Hz, 113.3 Hz, and 141.2 Hz. The reasons for this difference include two factors, the mass distribution and the structure stiffness. In the simulation model, the structure mass is hypothesized to be a concentrated load while the actual mass is distributed along the optical axis. Additionally, the mass in the simulation model is less than that of the actual instrument because some

Table 7
Test results of sinusoidal excitation.

Direction	Characteristic frequency	Mechanical amplification factor	Response
X	66.95	5.29	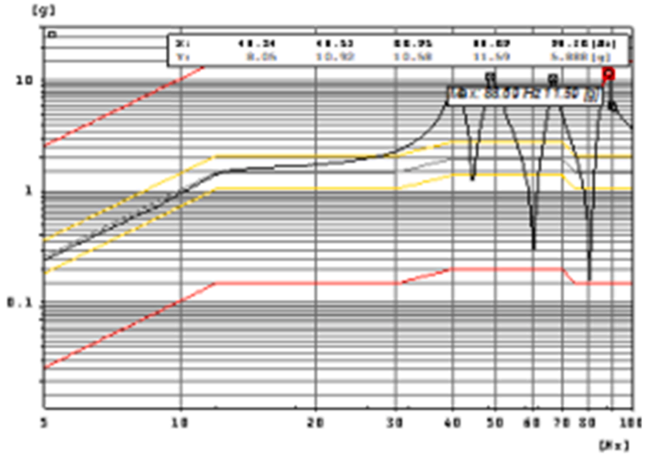
Y	98.84	4.058	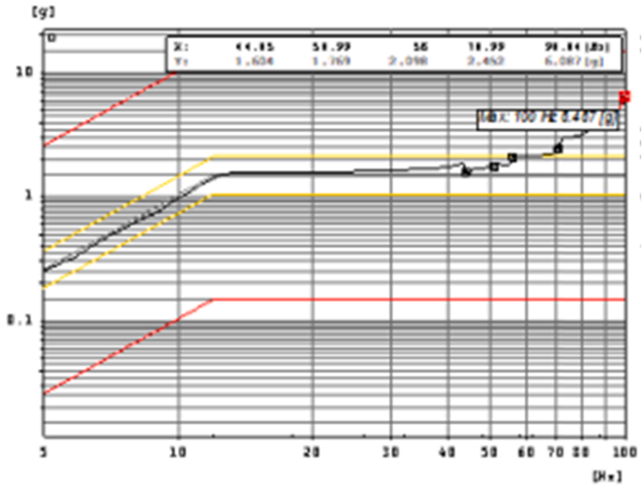
Z	70.37	6.537	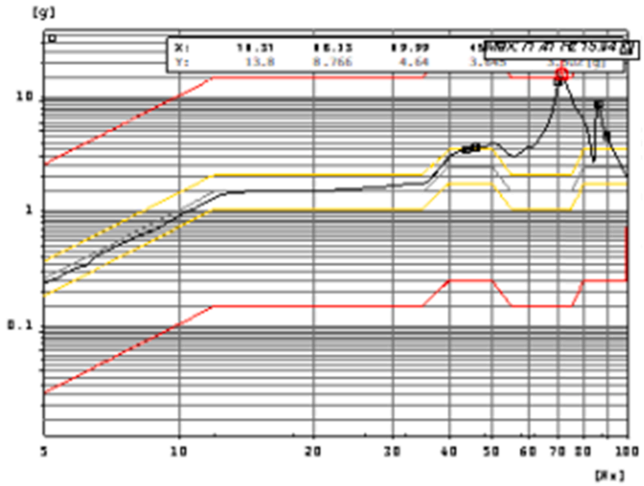

auxiliary components like cable racks and thermal control unit are not included in the simulation model. As to the stiffness, the multiple points constrain is used to simulate the connection between two mechanical components, which enhances the model stiffness and the characteristic frequency. In the actual test, the components are connected by bolts which are more flexible compared with multiple points constrain. That is why the characteristic frequencies in the test are 30–40 Hz less than that in the simulation. Moreover, the mechanical amplification factors on each direction are no more than seven, the dynamic load caused by which will not damage the structure according to engineering experience, so the material strength of the whole structure can meet the requirement.

6. Conclusion

CFRP is one of the most widely employed lightweight materials with high modulus. In this paper, fiber orientation and topology optimization are accomplished and optimum design result is acquired. The optimization algorithm of fiber orientation is verified by theoretical analysis and simulations, illustrating that $[90^{\circ}/+45^{\circ}/-45^{\circ}/0^{\circ}]$ fiber orientation and symmetrical laminas are indispensable such that the stiffness and strength of CFRP can be maximized and coupling stiffness matrix can be avoided. Additionally, the topology optimization algorithm is validated to be convergent and can provide a conceptual model which offers a reference for the critical design. Finally, the first three characteristic frequencies of the optical remote sensor are respectively 66.95 Hz, 70.37 Hz, and 98.84 Hz. The mechanical amplification factor of the first characteristic frequency is 5.29 in the mechanical test, which meet the performance requirement of the stiffness and strength for the optical remote sensor.

Declaration of Competing Interest

The authors declare that they have no known competing financial interests or personal relationships that could have appeared to influence the work reported in this paper.

Data Availability

No data was used for the research described in the article.

References

[1] C. Wu, Y.K. Gao, J.G. Fang, E. Lund, Q. Li, Discrete topology optimization of ply orientation for a carbon fiber reinforced plastic (CFRP) laminate vehicle door, Mater. Des. 128 (2017) 9–19.
[2] Z.K. Awad, T. Aravinthan, Y. Zhuge, F. Gonzalez, A review of optimization techniques used in the design of fiber composite structures for civil engineering applications, Mater. Des. 33 (2012) 534–544.
[3] J. Fang, Y. Gao, G. Sun, C. Xu, Q. Li, Multi-objective sequential optimization for a vehicle door using hybrid materials tailor-welded structures, Proc. Inst. Mech. Eng. Cj. Mech. Eng. Sci. 230 (17) (2015) 3092–3100.
[4] M.E. Botkin, Modeling and optimal design of a carbon fiber reinforced composite automotive roof, Eng. Comput. 16 (1) (2000) 16–23.
[5] R. Matsuzaki, K. Mitsui, Y. Hirano, A. Todoroki, Y. Suzuki, Optimization of curvilinear fiber orientation of composite plates and its experimental validation, Compos. Struct. 255 (2021), 112956.
[6] C. Nguyen, Y. Choi, Concurrent density distribution and build orientation optimization of additively manufactured functionally graded lattice structures, Comput. -Aided Des. 127 (2020), 102884.
[7] B. Krour, F. Bernard, A. Tounsi, Fibers orientation optimization for concrete beam strengthened with a CFRP bonded plate: a coupled analytical-numerical investigation, Eng. Struct. 56 (2013) 218–227.
[8] Z. Rasheva, G. Zhang, Th Burkhart, A correlation between the tribological and mechanical properties of short carbon fibers reinforced PEEK materials with different fiber orientations, Tribology Int. 43 (2010) 1430–1437.
[9] R. Voss, L. Seeholzer, F. Kuster, K. Wegener, Analytical force model for orthogonal machining of unidirectional carbon fibre reinforced polymers (CFRP) as a function of the fibre orientation, J. Mater. Process. Tech. 263 (2019) 440–469.
[10] P. Naghipour, M. Bartsch, L. Chernova, J. Hausmann, H. Voggenreiter, Effect of fiber angle orientation and stacking sequence on mixed mode fracture toughness of carbon fiber reinforced plastics: Numerical and experimental investigations, Mater. Sci. Eng. A 527 (2010) 509–517.
[11] H. Tang, Z.X. Chen, G.W. Zhou, Effect of fiber orientation distribution on constant fatigue life diagram of chopped carbon fiber chip-reinforced Sheet Molding Compound (SMC) composite, Int. J. Fatigue 125 (2019) 394–405.
[12] G.C. Papanicolaou, S.P. Zaoutsos, E.A. Kontou, Fiber orientation dependence of continous carbon/epoxy composites nonlinear viscoelastic behavior, Compos. Sci. Technol. 64 (2004) 2535–2545.
[13] M. Fotouhi, M. Jalalvand, M.R. Wisnom, High performance quasi-isotropic thin-ply carbon/glass hybrid composites with pseudo-ductile behavior in all fiber orientations, Compos. Sci. Technol. 152 (2017) 101–110.
[14] P. Wang, H.B. Zhang, J. Yin, X. Xiong, C.Y. Deng, Effects of fiber orientation on wear behavior of copper mesh modified carbon/carbon composite under electric current, Tribology Int. 116 (2017) 310–319.
[15] L. Quagliato, J. Lee, J.H. Fonseca, D. Han, H. Lee, Influences of stress triaxiality and local fiber orientation on the failure strain for injection-molded carbon fiber reinforced polyamide-6, Eng. Fract. Mech. 250 (2021), 107784.
[16] K.A. Calzada, S.G. Kapoor, R.E. DeVor, J. Samuel, A.K. Srivastava, Modeling and interpolation of fiber orientation-based failure mechanism in matching of carbon fiber-reinforced polymer composites, J. Manuf. Process 14 (2012) 141–149.
[17] H.C. Tseng, R.Y. Chang, C.H. Hsu, Numerical prediction of fiber orientation and mechanical performance for short/long glass and carbon fiber-reinforced composites, Compos. Sci. Technol. 144 (2017) 51–56.
[18] L.F. Yi, T. Yamamoto, T. Onda, Z.C. Chen, Orientation control of carbon fibers and enhanced thermal/mechanical properties of hot-extruded carbon fibers/aluminum composites, Diam. Relat. Mater. 116 (2021), 108432.
[19] B.X. Bie, J.Y. Huang, D. Fan, T. Sun, Orientation-dependent tensile deformation and damage of a T700 carbon fiber/epoxy composite: a synchrotron-based study, Carbon 121 (2017) 127–133.
[20] Z. Zhang, S.J. Hou, Y.Q. Mao, L.P. He, X. Han, Rate-related study on the ply orientation of carbon fiber reinforced epoxy composite laminates, Int. J. Mech. Sci. 188 (2020), 105968.
[21] H.Q. Ding, B. Xu, A novel discrete-continuous material orientation optimization model for stiffness-based concurrent design of fiber composite, Compos. Struct. 273 (2021), 114288.
[22] C.Y. Kiyono, E.C.N. Silva, J.N. Reddy, A novel fiber optimization method based on Normal Distribution Function with continuously varying fiber path, Compos. Struct. 160 (1) (2017) 503–515.
[23] E. Lund, J. Stegmann, On structural optimization of composite shell structures using a discrete constitutive parameterization, Wind Energy 8 (1) (2005) 109–124.

[24] K. Svanberg, A class of globally convergent optimization methods based on conservative convex separable approximations, SIAM J. Optim. 12 (2) (2002) 555–573.
[25] J.D. Deaton, R.V. Grandhi, A survey of structural and multidisciplinary continuum topology optimization: post 2000, Struct. Multidisc. Optim. 49 (2014) 1–38.
[26] J. Chun, G.H. Paulino, J. Song, Reliability-based topology optimization by ground structure method employing a discrete filtering technique, Struct. Multidiscip. Optim. 60 (2019) 1035–1058.
[27] T. Zegard, G.H. Paulino, Ground structure based topology optimization for arbitrary 3D domains using MATLAB, Struct. Multidisci. Optim. 52 (6) (2015) 1161–1184.
[28] Jr. Ramos, G.H. Paulino, Filtering structures out of ground structures-a discrete filtering tool for structural design optimization, Struct. Multidiscip. Optim. 54 (1) (2016) 95–116.
[29] J. Song, Y.J. Wang, W.Z. Zhou, R. Fan, B. Yu, Y. Lu, L.X. Li, Topology optimization guided lattice composites and their mechanical characteristics, Compos. Part B 160 (2019) 402–411.
[30] V.S. Papapetrous, C. Patel, A.Y. Tamijani, Stiffness-based optimization framework for the topology and fiber paths of continuous fiber composites, Compos. Part B 183 (2020), 107681.
[31] K. Suzuki, N. Kikuchi, A homogenization method for shape and topology optimization, Comput. Methods Appl. Mech. Eng. 93 (1991) 291–318.
[32] F. Belblidia, J.E.B. Lee, S. Rechak, E. Hinton, Topology optimization of plate structures using a single- or three- layered artificial material model, Adv. Eng. Softw. 32 (2001) 159–168.
[33] F. Fernandez, A.T. Barker, J. Kudo, J.P. Lewicki, K. Swartz, Simultaneous material, shape and topology optimization, Comput. Methods Appl. Engrg. 371 (2020), 113321.
[34] Evolutionary topology optimization of continuum structures with stress constraints, Struct. Multidiscip. Optim. 59 (2019) 647–658.
[35] D.J. Munk, T. Kipouros, G.A. Vio, G.T. Parks, G.P. Steven, Multi-objective and multi-physics topology optimization using an updated smart normal constraint bi-directional evolutionary structural optimization method, Struct. Multidisc. Optim. 57 (2018) 665–688.
[36] W.S. Zhang, J. Yuan, J. Zhang, X. Guo, A new topology optimization approach based on Moving Morphable Components (MMC) and the ersatz material model, Struct. Multidisc Optim. 53 (2016) 1243–1260.
[37] M. Otomori, T. Yamada, K. Izui, S. Nishiwaki, Matlab code for a level set-based topology optimization method using a reaction diffusion equation, Struct. Multidisc. Optim. 51 (2015) 1159–1172.
[38] S. Missoum, Z. Gurdal, S. Setoodeh, Study of a new local update scheme for cellular automata in structural design, Struct. Multidiscip. Optim. 29 (2) (2005) 103–112.
[39] K. Morimoto, A. Iguchi, Y. Tsuji, Efficient topology optimization of optical waveguide using finite element method based on slowly varying envelope approximation, Opt. -Int. J. Light Electron Opt. 226 (2021), 165951.
[40] P.F. Shi, Y.F. Tang, H.G. Zhao, R.J. Gao, S.T. Liu, Enhanced transmission through the topology optimized sub-wavelength aperture with maximum transmission efficiency, Opt. -Int. J. Light Electron Opt. 243 (2021), 167474.
[41] M. Stolpe, K. Svanberg, An alternative interpolation scheme for minimum compliance topology optimization, Struct. Multidiscip. Optim. 22 (2) (2001) 116–124.
[42] H. Liu, W.H. Zhang, T. Gao, A comparative study of dynamic analysis methods for structural topology optimization under harmonic force excitations, Struct. Multidisc Optim. 51 (2015) 1321–1333.
[43] J.B. Du, N. Olhoff, Topological design of freely vibrating continuum structures for maximum values of simple and multiple eigenfrequencies and frequency gaps, Struct. Multidisc Optim. 34 (2007) 91–110.
[44] K. Svanberg, The method of moving asymptotes-A new method for structural optimization, Int. J. Numer. Methods Eng. 24 (1987) 359–373.
[45] C. Zillober, A globally convergent version of the method of moving asymptotes, Struct. Optim. 6 (1993) 166–174.
[46] Y.Y. Liu, J.J. Dai, S.S. Zhao, J.H. Zhang, W.D. Shang, Optimization of five-parameter BRDF model based on hybrid GA-PSO algorithm, Opt. -Int. J. Light Electron Opt. 219 (2020), 164978.
[47] Z.S. Wang, Q.F. Guo, F. Jiang, B. Chen, Q.W. Wu, Stiffness design of cantilevered structure with space optics load, Opt. -Int. J. Light Electron Opt. 184 (2019) 330–338.
[48] Y. Khlifi, F. Al-Zahrani, All-optical core node modeling and optimization using hybrid wavelength conversion for QoS provision, Opt. -Int. J. Light Electron Opt. 231 (2021), 166374.